Selectively photocatalytic dehydrogenation of formic acid by in-situ restructured copper post-metalated metal organic framework under visible light

Houeida Issa Hamoud, Patrick Damacet, Dong Fan, Nisrine Assaad, Oleg Lebedev, Anna Krystianiak, Abdelaziz Gouda, Olivier Heintz, Marco Daturi, Guillaume Maurin, et al.

Selectively photocatalytic dehydrogenation of formic acid by in-situ restructured copper post-metalated metal organic framework under visible light

Houeida Issa Hamoud[†], Patrick Damacet[‡], Dong Fan, [‡‡] Nisrine Assaad[‡], Oleg Lebedev,[††] Anna Krystianiak,[‡†] Abdelaziz Gouda,[⊥] Olivier Heintz, [‡†] Marco Daturi[†], Guillaume Maurin,[‡‡] Mohamad Hmadeh[‡*], Mohamad El-Roz[†*].

[†] Normandie Univ, ENSICAEN, UNICAEN, CNRS, Laboratoire Catalyse et Spectrochimie, Caen 14050, France;
[‡] Department of Chemistry, American University of Beirut, P.O. Box 11-0236, Riad El-Solh, 1107 2020 Beirut, Lebanon
[††] Normandie Univ, ENSICAEN, UNICAEN, CNRS, Laboratoire CRISMAT, UMR 6508, 14050 Caen, France;
[⊥] Department of Chemistry University of Toronto, 80 St. George Street, Toronto, ON M5S 3H6, Canada
[‡‡] Institut Charles Gerhardt Montpellier (ICGM), University of Montpellier, CNRS, ENSCM, 34095 Montpellier, France.
[‡†] *ICB, CNRS UMR 6303 – Université de Bourgogne Franche-Comté, 9 Avenue A. Savary, 21078 Dijon, France*

KEYWORDS: Hydrogen, Photocatalysis, Operando FTIR, MOFs, Formic acid, Copper.

ABSTRACT: Formic acid is considered as one of the most promising liquid organic hydrogen carriers (LOHC). Its catalytic dehydrogenation processes generally suffer from low activity, low reaction selectivity, low stability of the catalysts and/or the use of noble-metal based catalysts. Herein, we report a highly selective, efficient, and noble metal-free photocatalyst for the dehydrogenation of formic acid. This catalyst is built from a post-metalation of a carboxylic-functionalized Zr-MOF by copper, namely UiO-66$(COOH)_2$-Cu. The visible light driven photocatalytic dehydrogenation process through the release of hydrogen and carbon dioxide is monitored in real-time via *operando* FTIR and reveals almost 100% of selectivity with high stability (over 3 days) and conversion yield exceeding 60% (around 5 $mmol.g^{-1}_{cat}.h^{-1}$) at ambient conditions. These performance indicators make UiO-66$(COOH)_2$-Cu among the top photocatalysts for formic acid dehydrogenation. Interestingly, the as-prepared UiO-66$(COOH)_2$-Cu hetero-nanostructure was found moderately active under solar irradiation during an induction phase, whereupon it undergoes an *in-situ* restructuring process through intra-framework cross-linking with the formation of the anhydride analogue structure, UiO-66$(COO)_2$-Cu, and nano-clustering of highly active and stable copper sites as evidenced by the *operando* studies coupled with steady state isotopic transient kinetic (SSITKA) experiment, TEM, XPS analysis and DFT calculations. Beyond revealing outstanding catalytic performance for UiO-66$(COO)_2$-Cu, this work delivers an in-depth understanding of the photocatalytic reaction mechanism implying an evolutive behavior of the post-metalated copper as well as the MOF framework over the reaction. These key findings pave the ways towards the engineering of new simple and efficient catalysts for photocatalytic dehydrogenation of formic acid.

Introduction

Hydrogen is one of the most basic and most abundant elements on this planet. However, it is rarely found in its molecular form, being essentially present in molecular compounds[1]. Therefore, it needs to be extracted through different processes. Molecular hydrogen has experienced a global resurgence lately as an energy carrier and a secondary source of green energy[2]. Despite being characterized by a small atomic weight, low boiling point, high flammability range, and extremely low density, it possesses an enormous gravimetric energy (chemical energy per unit mass) of 120 $kJ.g^{-1}$, which surpasses that of methane, gasoline, and ethanol standing only at about 56 kJ/g, 47 kJ/g, and 30 kJ/g respectively [3]. . Therefore, the development of cheap, safe, and effective hydrogen on-site catalytic production systems has been gaining much attention in the past few years[5, 6]. Along with the various thermal, photocatalytic, electrical, and biological processes utilized, including fermentation, bio-photolysis, alkaline electrolysis, and water splitting based solar energy, steam reforming processes are considered the most feasible route for hydrogen production[19]. In such processes, hydrogen is generated via catalyzed endothermic equilibrium reactions between a hydrocarbon (e.g. methanol, acetone, methane, formic acid and ethylene glycol) and steam[20].

Recently, formic acid (HCOOH) has been attracting much attention as a promising hydrogen source and liquid organic hydrogen carrier (LOHC) species [21-23]. This is due to its advantageous properties including its low toxicity, non-flammability, high stability, biodegradability, and availability where more than 600,000 megatons of formic acid are being produced worldwide on yearly-basis [5, 24]. In this

regard, formic acid is recognized as one of the most promising hydrogen carriers with an H_2 volumetric capacity of 53 $kg.m^{-3}$, that corresponds to a huge energy density of 1.76 $kW.h.L^{-1}$ [25]. What makes formic acid an excellent H_2 storage and production system is the fact that hydrogen release occurs spontaneously at mild conditions resulting in an exergonic process [26-28], as opposed to other carriers such as methanol, acetic acid, acetaldehyde, and ammonia that require temperatures above 373 K to release H_2, in addition to other drawbacks such as a poor selectivity where more than one major product can be obtained [29-31].

Formic acid, which contains approximately 4.4 weight percentage hydrogen, degrades in the absence of catalyst via two low-enthalpy routes associated with the following chemical reactions: [23]

Dehydrogenation (Decarboxylation): $HCOOH_{(l)} \rightarrow CO_2\ (g) + H_2\ (g) \quad \Delta G^0 = -32.9\ kJ.mol^{-1}$ equation 1

Dehydration (Decarbonylation): $HCOOH_{(l)} \rightarrow CO\ (g) + H_2O\ (g) \quad \Delta G^0 = -12.4\ kJ.mol^{-1}$ equation 2

The dehydrogenation of formic acid is a desired and indispensable pathway for all systems using this chemical species as a hydrogen storage and production medium. Although this route involves the generation of CO_2 along with H_2, the former can be thereafter hydrogenated using any appropriate catalyst resulting in the regeneration of formic acid via a carbon-free emission cycle [32-34]. On the other hand, the second route illustrated by the dehydration of formic acid is assumed to be undesired due to the fact that the generation of carbon monoxide (CO) results in the poisoning of the fuel cell's catalyst and leads to a lower overall hydrogen yield [35].

A tremendous amount of research has been conducted during the past few years on the development of convenient homogeneous and heterogeneous catalysts for formic acid dehydrogenation [36-38]. For instance, after Coffey initially reported the first homogeneous catalytic system based on Ru, Ir, and Pt phosphine complexes for the degradation of formic acid in 1967 [39], various research groups have been involved in the development and investigation of new active homogeneous catalysts based on noble metals, bipyridine moieties, and pincer type ligands. As for the heterogeneous systems, they are mostly made of metal oxides and supported metallic nanoparticles out of which noble metal-based catalysts are known to be the most efficient and sustainable ones in the latter category [40-44]. Although acceptable catalytic activities have been achieved using heterogeneous catalysts, their poor stabilities in acidic conditions were major concerns [45, 46]. Moreover, most metal oxides employed as photo or thermo-active catalysts including TiO_2 nanoparticles resulted in a low sustainability, low selectivity towards H_2, and formation of CO as a side product under mild conditions. [47, 48].

Metal organic frameworks (MOFs) are a new and promising class of crystalline porous hybrid materials composed of metal ions clusters linked to organic linkers via strong covalent bonds forming extended networks [49-51]. Due to their outstanding features including high internal surface area, large porosity, structural tunability, and potentially high density of active sites combined with acceptable thermal and chemical stability [52, 53], MOFs have attracted much attention in the field of heterogeneous catalysis [54-63]. They have been used as effective supports to immobilize metal nanoparticles in their pores and on the functional groups within the backbone of the framework which prevents the nanoparticles' aggregation [64].

There have been very few reports on the decomposition of formic acid to hydrogen and carbon dioxide using MOFs as catalysts to date. In particular, the incorporation of palladium and palladium-gold nanoparticles was achieved in two different MOF frameworks, MIL-125 and MIL-101 respectively [64, 65]. Although a good formic acid conversion was achieved over these MOF-based catalysts, their stability and selectivity were much lower than the existing homogeneous catalysts[27, 66]. Nevertheless, a high selectivity towards H_2 was achieved using a ruthenium complex immobilized on a newly synthesized phosphine-functionalized MOF known as LSK-15 however a moderate conversion rate was obtained at temperatures higher than 125°C [67].

Herein, we present a visible-light driven dehydrogenation of formic acid into H_2 over a copper-post-metalated zirconium-MOF, namely UiO-66-$(COOH)_2$-Cu. Remarkably, this engineered photocatalyst is demonstrated to be highly selective (>99.9%) and ultra-highly stable with a formic acid conversion of 60% at room temperature and 90% at 150 ^{0}C, achieved for three continuous days without losing efficiency and selectivity. Formic acid photo-conversion along with hydrogen and carbon dioxide evolutions are monitored in real time using *operando* FTIR, where isotopically enriched $H^{12}COOH/H^{13}COOH/D^{12}COOH$ reactants are employed to characterize the photo-activity and selectivity of the catalyst as well as to elucidate, in tandem with density functional theory (DFT) calculations, the catalytic reaction mechanism implying an uncommon evolutive behavior of both post-metalated Cu- species and MOF framework. Finally, the temperature-dependence of the kinetics and thermodynamics of the catalytic reaction is systematically examined to assess the promises of the catalysts for further applications.

Experimental section

Materials

All chemical reagents and solvents mentioned in this work were commercially supplied and used directly without any additional purification. Zirconyl chloride octahydrate ($ZrOCl_2.8H_2O$), 1,2,4,5-benzenetetracarboxylic acid, methanol (gradient grade, 99,93%),dimethylformamide (ACS grade) and copper (II) nitrate were purchased from Sigma Aldrich.

Synthesis of UiO-66$(COOH)_2$

UiO-66$(COOH)_2$ was synthesized under conditions similar to those reported in the literature [68]. In brief, an equimolar amount of zirconyl chloride octahydrate (59.4 mg, 0.184 mmol) and 1,2,4,5-benzenetetracarboxylic acid (47.1 mg, 0.184 mmol) were dissolved in 4 mL of DMF already placed in a 20 mL scintillation vial and sonicated for a couple of minutes. 4 mL of formic acid modulator was later added to the obtained mixture followed by sonication for few extra minutes. The reaction mixture was then

placed in a pre-heated oven at 130^{0}C for 5 hours. The obtained white powder was collected by centrifugation at 4000 rpm and washed five times with DMF and three times with MeOH. UiO-66(COOH)$_2$ was then dried under dynamic vacuum oven at 110^{0}C overnight.

Preparation of UiO-66(COOH)$_2$-Cu

In a 20 mL scintillation vial, 30 mg of copper nitrate was dissolved in 15 mL of DMF by sonication for 10 mins until a clear solution was obtained. 60 mg of UiO-66(COOH)$_2$ was then added to the copper solution and sonicated for few minutes to ensure full MOF dispersion in the solution. The mixture was then stirred on a hot plate at 75°C for 21hrs until brownish microcrystalline powder was obtained. The supernatant was discarded by centrifugation and the solids were washed with DMF for 2 days with fresh DMF being exchanged 3 times per day followed by fresh methanol for another 2 days. Finally, the solids were collected by centrifugation and dried in a vacuum oven at 80°C overnight.

Characterization

Powder X-Ray Diffraction (PXRD) analyses of UiO-66-(COOH)$_2$ and UiO-66-(COOH)$_2$-Cu were carried out using a Bruker D8 advance X-ray diffractometer with a Cu Kα radiation (k=1.5418 Å) a 40 kV voltage, and a 40 mA current, while the 2θ range was between 5-50°, at an increment of 0.02° (Bruker AXS GmbH, Karlsruhe, Germany). Nitrogen adsorption/desorption measurements were performed with an ASAP 2020 MP instrument. The specific surface area was calculated with the BET equation, while the pore volumes were determined by the BJH method. Prior to the measurements, samples were activated under dynamic vacuum at 110 ºC for 6 h. The content and distribution of Cu and Zr were determined by Scanning electron microscopy-energy dispersive X-ray (SEM-EDS) on a JEOL, JSM-5500LV microscope or a MIRA TESCAN microscope. The images were collected with an acceleration voltage of 30 kV. The amount of copper incorporated in the framework was determined by iCE 3000 series atomic absorption spectrophotometer (AAS) by digesting the catalyst in aqua regia and hydrofluoric acid (HF) solutions (more details in SI).

X-ray photoelectron spectroscopy (XPS) measurements were carried out on an Versaprobe electron spectrometer (ULVAC-PHI) with base vacuum in the analysis chamber in the order of 10^{-8} Pa. The samples are irradiated with monochromatized Al Kα radiation with photon energy of 1486.6 eV. The resolution measured by the FWHM of Ag $3d_{5/2}$ line is 0.6 eV for the setting used during acquisitions. Energy calibration was performed on the C 1s line of adventitious carbon at 284.8 eV. CasaXPS is used for data treatment Advanced transmission electron microscopy (TEM) was carried out on an aberration probe, and image corrected JEM ARM200F cold FEG microscope operated at 200 kV equipped with a CENTURIO EDX detector and GIF Quantum spectrometer. DR-UV-Vis measurements relevant to Cu's speciation and oxidation state were carried using a Cary 4000 UV-Vis spectrophotometer and a HARRICK praying Mantis diffuse reflectance accessory. All spectra were recorded between 200-800 nm using an average time of 0.2 s and a scan rate of 300 nm/min.

Nanosecond transient absorption experiments were performed using a commercial transient absorption spectrometer (Edinburgh Instruments; LP 980) pumped with a nanosecond 10 Hz Nd:YAG laser and harmonic crystals (266 nm; 355 nm and 532 nm). The samples were collected at a rate of 1 Hz and prepared in a 1 × 1 cm quartz cuvette to an absorbance value around 0.2 OD of dispersed MOF (around 1 mg) in dry CH_3CN.

Photocatalytic test

For the *operando* experiments, a 'Sandwich' IR cell-reactor (Scheme S1) was used to study the performance of the UiO66-(COOH)$_2$ and its Cu-metalated derivative during the photodecomposition of formic acid (FA) under visible irradiation at room temperature (RT = 25 °C). The catalyst, as a self-supported pellet of about 20 mg, was first activated in Ar at RT under visible irradiations using a Xe-lamp (LC8 Hamamatsu, 71 mW/cm^2 of irradiance) with a pass-high filter >390 nm. Then, the reaction was studied in the presence of 2400 ppm of FAc with a total flow rate of 25 cc.min^{-1} in Argon. Additional tests were performed in the presence of FAc-^{13}C and DCOOH. The relative concentrations of the effluent gas were stabilized before being sent to the cell, then an adsorption step of formic acid on the catalyst surface was performed in dark before turning on the lamp. Finally, the composition of the output gas from the IR reactor cell was analyzed simultaneously by Mass Spectrometry (Quadrupole Pfeiffer Omnistar GSD 301) and IR spectroscopy (ThermoNicolet NEXUS 670 FTIR) equipped with a MCT detector with a spectral resolution of 4 cm^{-1} and accumulating 64 scans. The concentration of formic acid (FA) in the gas phase was calculated using the surface area of the IR band at 1109–1101 cm^{-1} and the formic acid MS signal (m/z = 45 and 46). The CO_2 and CO selectivity's were determined using the IR band area at 2395-2182 cm^{-1} and 2140-2020 cm^{-1}, respectively. The amounts of hydrogen were determined by its MS signal at m/z = 2 after correction from water contributions. The formic acid conversion (expressed in % or mmol per g of photocatalyst per irradiated surface) and the selectivity (%) were calculated at the steady-state using the calibration curve for different product of the reaction. It should be noted that the irradiated surface of the pellet is about 1.6 cm^2 (~ 20 % of the total surface (2 cm^2) is not irradiated due to the metallic holder shadow effect).

Computational methods

To account for the formation of the anhydride form of the Cu-metalated MOF evidenced experimentally upon light irradiation and formic acid adsorption, we adopted our previously constructed anhydride model for UiO-66-(COOH)$_2$ labeled as UiO-66-(COO)$_2$ with anhydride bridge formed between adjacent ligands[69]. All the calculations for the reaction process were realized on a representative cluster model UiO-66-(COO)$_2$ loaded with a single Cu as model system as shown in Figure S1 and noted thereafter UiO-66-(COO)$_2$-Cu. All DFT computations were performed by using the Vienna *Ab-initio* Simulation Package (VASP,

version: 5.4.4)[70] with the Projector augmented-wave (PAW) method to describe the pseudopotential. The electron exchange-correlation functional was treated by the Perdew–Burke–Ernzerhof functional within the generalized gradient approximation (GGA) scheme[71]. The energy cutoff of the plane wave was set to 520 eV with an energy (force) precision of 10^{-5} eV (0.01 eV per Å). The van der Waals interaction was also included by using Grimme's DFT-D3 method[72]. The Brillouin zone was sampled with a 1 × 1 × 1 Monkhorst–Pack *k*-points grid for geometry optimization. Transition state of the reaction was confirmed by using the Climbing-Image Nudged Elastic Band (CI-NEB) approach[73]. To evaluate the adsorption strength of intermediates and the catalytic performance of each elementary step, the Gibbs free energy change (ΔG) relative to the total free energy of UiO-66-$(COO)_2$-Cu and gas-phase HCOOH was calculated using the following equation (equation 3):

$$\Delta G = \Delta E_{DFT} + \Delta E_{ZPE} - T \times \Delta S \quad \text{equation 3}$$

where ΔE_{DFT} , ΔE_{ZPE}, T and ΔS are the DFT calculated electronic energy, zero-point energy, environmental temperature (298.15 K) and entropy, respectively.

Results and discussion

MOF catalyst synthesis and characterization

UiO-66-$(COOH)_2$ MOF crystals were solvothermally synthesized using formic acid as modulator according to a previously published procedure[68]. As for the metalation, copper nitrate was employed as metal source which was added to the UiO-66-$(COOH)_2$ crystals dispersed in DMF at 75 °C overnight. AAS was used to quantify the amount of copper incorporated in the framework and found to be 18%. Scanning electron microscopy (SEM) images and energy-dispersive X-ray (EDX) mapping analyses further confirmed the successful metalation of UiO-66-$(COOH)_2$ and revealed a homogeneous distribution of metal sites and the coexistence of Zr and Cu in all crystals (Figure 1). The obtained ratio from EDX analysis was also in agreement with the AA results. PXRD patterns were recorded before and after metalation and demonstrated the phase purity and the high crystallinity of UiO66-$(COOH)_2$ (Figure 1). Furthermore, no additional peaks related to crystalline copper species were observed, which confirmed that copper was anchored to the framework in its cationic form. The oxidation state and the form of the copper species will be discussed further in the photocatalytic reaction section. In order to assess the porosity of the synthesized MOF catalyst, N_2 isotherms were performed on UiO66-$(COOH)_2$ and its Cu-metalated derivative (Figure S2). The obtained isotherms are of type I, which indicate the microporous nature of the samples. The BET surface areas were measured to be 240 $m^2.g^{-1}$ and 48 $m^2.g^{-1}$ for UiO66-$(COOH)_2$ and UiO66-$(COOH)_2$-Cu, respectively. This decrease in the BET surface area is the result of the post-metalation process. A decrease in the pore volumes was observed as well, with UiO-66$(COOH)_2$ showing a pore volume of 0.16 $cm^3.g^{-1}$ compared to 0.05 $cm^3.g^{-1}$ for the copper-post-metalated MOF.

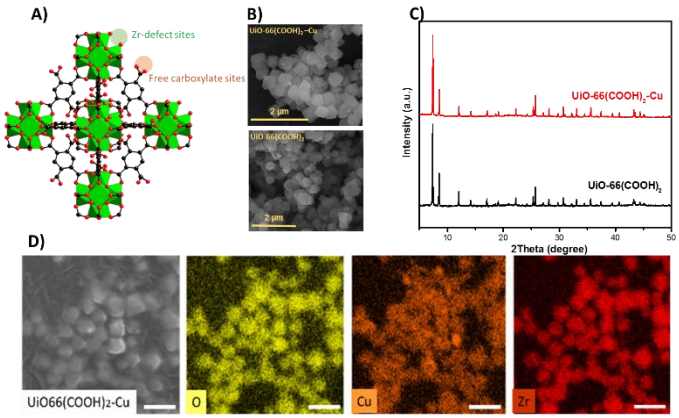

Fig 1. A) Structure of UiO-66$(COOH)_2$ showing the possible anchoring sites for Cu (Zr open metal sites created by missing linkers and free carboxylic functions). B) SEM images of UiO-66$(COOH)_2$ crystals before and after copper metalation. C) Powder X-ray diffraction patterns of UiO-66$(COOH)_2$ compared to its metalated form. D) EDX mapping of UiO-66$(COOH)_2$-Cu showing the distribution of Cu and Zr in the MOF crystals.

Activity, selectivity, and stability of the UiO66 based photocatalysts

The photocatalytic performance of UiO66-$(COOH)_2$-Cu for the dehydrogenation of formic acid was tested under flow conditions (25 $cm^3.min^{-1}$ with 0.25% of HCOOH in Ar) and visible-light irradiation using an operando IR reactor[74] (Scheme S1). This reactor allows investigating simultaneously and in real time the modification on the photocatalyst surface as well as the reaction gas phase. The amounts of CO_2 and H_2 produced from this reaction were analyzed by gas-FTIR spectroscopy and/or mass spectrometer, respectively. In order to verify the origin of the produced CO_2, a C-13 labeled formic acid ($H^{13}COOH$) reactant was used. The evolution of the formic acid conversion over time demonstrates an increase in the first minutes of irradiation before reaching a steady state after 25 minutes (Figure 2A). Similar trend is observed for $^{13}CO_2$, with traces of $^{12}CO_2$ (5 to ~1% at steady state) detected in the first minutes of irradiation (Figure 2B-C). The latter is probably originated from the residual formic acid used during the UiO66-$(COOH)_2$ synthesis in addition to the $H^{12}COOH$ impurity (1%) already present in the $H^{13}COOH$ sample. The selective production of $^{13}CO_2$ at steady state demonstrates the photocatalytic dehydrogenation of the ^{13}C labeled formic acid and the photostability of the UiO66-$(COOH)_2$-Cu catalyst during the reaction under the operating condition.

Decisively and based on the carbon balance, the selectivity of the formic acid dehydrogenation in this reaction was found to be more than 99%, where no CO was detected in the gas phase of the reaction. This outcome is also confirmed by an equimolar production of H_2 and CO_2 at the steady state. Remarkably, during the first hundred minutes of the reaction, the H_2 evolution follows a different profile than that of formic acid conversion and CO_2 production. This trend is unusual for a pure photocatalytic dehydrogenation process where each molecule of CO_2 should be accompanied with a molecule of H_2 (Figure 2B-C). The

experiment was repeated four times and this behavior was completely reproducible. This observation suggests a possible interaction between FAc and the MOF structure at the beginning of the reaction under visible light irradiation. IR analysis of the photocatalyst surface demonstrates the appearance of new bands at around 1855, 1798 and 1785 cm^{-1} in the first minutes of the photocatalytic reaction (Figure 2D). These bands are characteristic of anhydride functions which were previously observed during the thermal activation of UiO66-$(COOH)_2$.[69] Indeed, Clet et *al.* attributed these bands to the thermal dehydration of the free carboxylic groups of the MOF structure, resulting in the formation of the bridged anhydrides at relatively high temperature (>100°C). The resulting structure is labeled as UiO66-$(COO)_2$-Cu. For comparison, the IR spectra of the sample before and after 20 minutes of visible-light activation at 25 °C under pure Ar carrier gas (FAc-Free) demonstrated only a complete removal of the adsorbed water from the surface of the catalyst without detecting the characteristic anhydride bands. In addition, only the bands of adsorbed HCOOH are detected at the steadystate after HCOOH adsorption (Figure S3). These reference tests explain the delay between the CO_2 and H_2 production, where the formic acid's protons could be involved in the restructuring of UiO66-$(COOH)_2$-Cu to UiO66-$(COO)_2$-Cu.

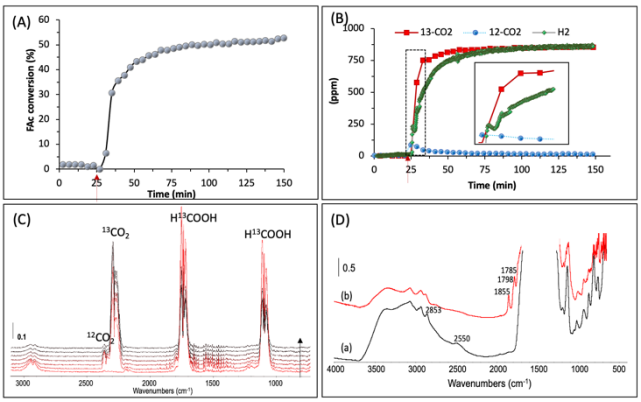

Figure 2. Evolution of the formic acid conversion (A), of the $^{13}CO_2$,$^{12}CO_2$ and H_2 quantities during the HCOOH reforming (inset: zooming on the first minutes of reaction, the arrows correspond to the light-on time) (B) and of the evolution FTIR spectra of the reaction gas-phase during the first minutes (4 min/spectrum) of the reaction (C). FTIR spectra of UiO66-$(COOH)_2$-Cu sample at steady state in dark (a) and (b) during the reforming of HCOOH (labeled with C-13 at 99% (H_2O<5%)) under visible light irradiation (D). Reaction conditions: total flow 25 cc/min; [HCOOH-^{13}C]=2400ppm (0.24%) in Ar; T=25°C; Xe-lamp 150 W with visible light pass filter λ>390 nm); irradiance=71 mW/cm²; m_{cat}=20 mg (self-supported pellet with surface of 1.6 cm²).

Before the *in-depth* characterization of the restructuring phenomena, the stability of the photocatalyst was tested in three photocatalytic cycles for around 24 hours for each (Figure 3). The results demonstrate an ultra-high stability of the sample during the reaction for three successive days without any significant deactivation while maintaining 100% of selectivity (no detection of CO; Figure 2C). Moreover, the structural and chemical stability of the samples were confirmed by PXRD and Raman spectroscopy showing no significant structural modification of the samples after reaction with respect to the as synthesized sample (Figure S4), while the characteristic anhydride bands reached a steady state after the first cycle. To the best of our knowledge, such high photocatalytic stability has never been reported so far for a MOF when this later is used as photocatalyst in vapor and acidic medium. Interestingly in sharp contrast with the first cycle where H_2 evolution follows a different profile than that of formic acid conversion and CO_2 production, the second and the third cycles reveal H_2 production quantities that match the HCOOH conversion and CO_2 production amounts, reaching quickly the steady state without any significant induction time (Figure 3). This strongly suggests that in the same way as for the formation of anhydride, restructuring of UiO66-$(COOH)_2$-Cu to UiO66-$(COO)_2$-Cu only occurs at the 1st cycle and no substantial changes are observed for the following cycles. Moreover, the decrease of H_2 in the beginning of cycles 2 and 3 is due to a higher covering surface of the photocatalyst by formic acid in the dark and before reaching a new equilibrium under irradiation conditions at the steady state. The great difference in FAc conversion at the beginning of the dark cycles is due to the adsorption of formic acid rather than its conversion.

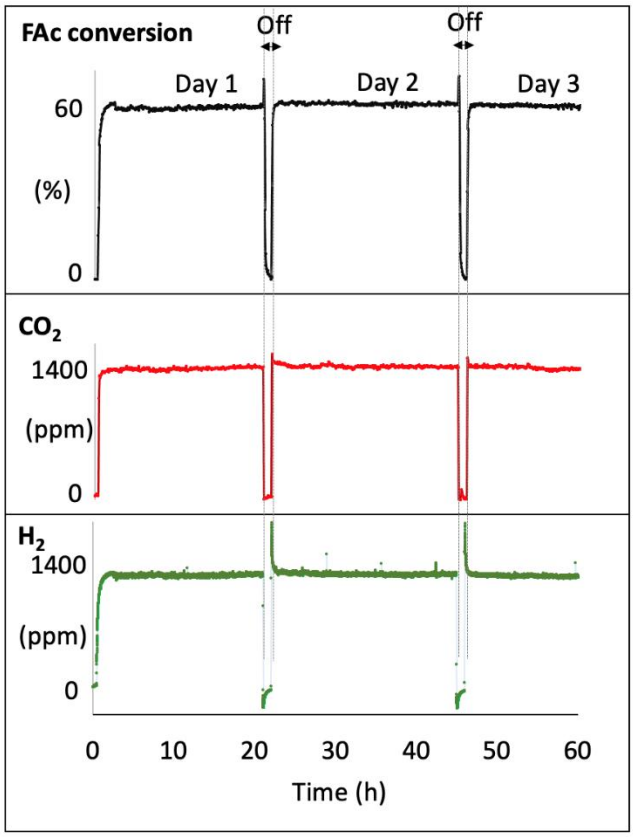

Figure 3. Evolution of the HCOOH conversion and the corresponding gas phase products during three cycles/days. The regions designated by arrows correspond to the dark stages. Reaction condition: total flow 25 cc/min; [HCOOH-^{13}C]=2400ppm (0.24%) in Ar; T=25°C; Xe-lamp 150 W with visible light pass filter (λ>390 nm); irradiance=71 mW/cm²; m_{cat}=20 mg (self-supported pellet with a surface of 1.6 cm²).

The thermal activity of the UiO66-$(COO)_2$-Cu and the temperature effect on its photocatalytic performance were further investigated and the obtained results are shown in Figure 4. As it can be clearly seen, no significant thermo-activity is observed in dark below 100°C and the activity is very low between 100°C and 150°C (Figure 4A). However, the temperature increase enhances the photocatalytic activity of the sample under visible light to reach 90% of formic acid conversion at 150 °C while maintaining a 100% selectivity with the formation of only CO_2 and H_2 (Figure 4B). Nevertheless, after the test performed at 150°C, the sample was cooled back and tested at room temperature and the results were compared with those obtained at room temperature with a fresh sample (Figure S5). A significant drop on the activity is observed demonstrating a low stability of the UiO66-$(COO)_2$-Cu at relatively high temperature in presence of FAc. The low activity of the sample in dark demonstrates the main photocatalytic nature of the reaction using UiO66-$(COO)_2$-Cu.

Additionally, the apparent quantum yield of UiO-66-$(COOH)_2$-Cu of hydrogen production is determined based on the procedure and equations presented in the SI document and is found to be 10.6 % (Figure S6) which is relatively high for a vapor/solid phases heterogeneous photocatalytic reaction.

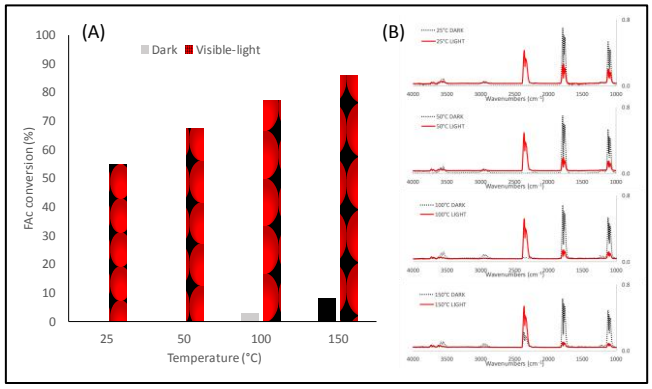

Figure 4. (A) Effect of the temperature on the FAc reforming in dark and under visible light irradiation. (B) the corresponding IR spectra of the reaction gas phase at the steady state at the studied at temperatures between 25 °C (top) and 150 °C (bottom). Reaction conditions: total flow 25 cc/min; [Fac-^{13}C]=2400 ppm (0.24%) in Ar; Xe-lamp 150 W with visible light pass filter (λ >390 nm); irradiance = 71 mW/cm^2; m_{cat} =20 mg (self-supported pellet with surface of 1.6 cm^2).

Role of the Cu in the photocatalytic dehydrogenation

In order to better understand the effect of the copper sites and the UiO66-$(COOH)_2$ framework structure on the activity, Cu-free UiO66-$(COOH)_2$,UiO66$(COOH)_2$-M (M = Ag, Co), and Cu-metalated non-functionalized UiO-66 (UiO66-Cu) are prepared and tested under similar reaction conditions to UiO66-$(COOH)_2$-Cu. The Cu-free UiO66-$(COOH)_2$ sample does not show any significant activity under visible light as well as under UV irradiation (Figure S7). This confirms that Zr metal centers of UiO66-$(COOH)_2$ have a passive role in the formic acid reforming and can be excluded as catalytic active sites. Moreover, Ag-, and Co- metalated UiO66-$(COOH)_2$ exhibit 4.6, and 6.4 -fold lower catalytic activities than the copper metalated MOF, respectively (Figures S8 and S9). Regarding the UiO66-Cu sample, Cu cations are expected to be inserted in the vicinity of the defective sites of the Zr-cluster[75] and their content was 8 wt.% as determined via AAS. The UV spectrum shows similar optical behavior for UiO66-Cu and UiO66-$(COOH)_2$-Cu (Figure S10A). The photocatalytic test using UiO66-Cu reveals a much lower activity (8.8 % HCOOH conversion) and poorer H_2/CO_2-selectivity compared to UiO66-$(COO)_2$-Cu (60% vs. 100%, respectively) as seen in figure S7. Indeed, these observations support that the copper coordinated to the functional groups of UiO66-$(COOH)_2$/UiO66-$(COO)_2$ plays a predominant role in the photocatalytic dehydrogenation of the formic acid. Furthermore, the copper content in UiO-66-$(COOH)_2$-Cu was varied and three batches of 6 wt. %, 9 wt. % and 16 copper wt. % were tested. It is noteworthy that higher percentage of copper loading was not possible. Indeed, a maximum of 16% can be achieved for our UiO-66$(COOH)_2$ sample, beyond which Cu cations are washed out throughout the purification process. The obtained results are shown in (Figures S11 and S12) and demonstrate that with the increase in copper content from 6 wt. % to 9 wt. % accompanied with an increase of the selectivity and the activity of the MOF increased from 43 % to 47.5 % to finally reach 65.5 % of FAc conversion for the 16 wt. % Cu-loaded sample. These results show that even at low copper loading (6 w%), the activity is still higher than the other metalated versions (e.g. Ni, Co and Ag of higher metal content). More importantly, the 6 wt. % UiO-66-$(COOH)_2$-Cu is 5-folds more active than the non-functionalized system (UiO-66-Cu with 8 wt. % of Cu), which means that the free carboxylates are thermodynamically favored for copper metalation and formation of active species. Figure S12 also shows that the selectivity is significantly affected at low Cu loading where CO was detected with a selectivity around 10%. Moreover, only few ppb of Co is permitted in H_2 fuel cell for preventing the poisoning of the catalyst making the high loaded Cu sample as most promising catalyst.

In addition, Cu-MOF-74, which incorporate copper rod secondary building units, CuO and Cu_2O nanoparticles were also tested under similar reaction conditions. While no to little activities of CuO and Cu-MOF-74 are observed, Cu_2O shows a very low activity (5.6% conversion) indicating the synergic effect between the copper centers and the framework in addition to the importance of the UiO66-$(COOH)_2$ structure in the photocatalytic reaction (Figure S7, Table S1). Noteworthily, the high catalytic performance, stability, and selectivity of the noble metal-free UiO-66-$(COO)_2$-Cu photocatalyst in the dehydrogenation of formic acid is comparable to most homogeneous and heterogeneous photocatalysts reported in literature (table S2). Due to the various possible experimental conditions that can be used for this reaction (irradiation source, light intensity, temperature, irradiated surface of photocatalyst, reactor geometry, mass of the photocatalyst, etc...), in addition to missing information in some of the reported works (stability of the catalyst, irradiance, selectivity, etc.), we

believe that the comparison is mostly indicative and not quantitative. Nevertheless, the data found in the literature which are now listed in table S2, show that our work is the first on the reforming of formic acid in the "vapor" phase under "continuous" flow which is totally innovative, and show the highest activity in comparison with other Cu-based photocatalyst under visible light and at ambient temperature.

Moreover, the optical band gap energies Eg for the free and copper metalated MOFs were determined from the absorbance data using the Tauc-plot method (fig S10B, and C), As expected, the calculated Eg for UiO66-$(COOH)_2$ was 3.9 eV. However, in the case of UiO-66-$(COOH_2)$-Cu (Figure 10C), the in-situ formation of $Cu^{(I)}$ oxa nanoparticles was evident by the narrow band gap observed (Eg=1.84 eV) which corresponds to the band gap of Cu_2O semiconductor [76].

The charge transfer (CT) between the UiO66-COOH structure and the copper site is also investigated by absorption transient spectroscopy. The results presented in Figure (S13A) demonstrate no absorption transient (AT) of the post metalated MOF structure $(UiO66\text{-}COOH)_2$ with a high photoluminescence (PL). However, UiO66-$(COOH)_2$-Cu exhibits an AT decay (broad AT band with a maximum at 440 nm) with very low PL emission, confirming a CT between the MOF structure and the Cu centers. Increasing the FAc concentration (Figure S13B) led to a leaching of the Cu sites as demonstrated by the decrease of the AT intensities. These results figure out an important role of the MOF structures, beyond a simple host of the Cu, in the initiation of the in-situ structuring of the Cu sites. Cyclic voltammetry (CV) was performed in 0.5 M Na_2SO_4 to reveal the redox reaction of the Cu species in the MOF structure (Figures S14A). CV of UiO-66-$(COOH)_2$Cu depicts redox features at ca. 0.129 V, 0.015 V and -0.643 V vs Ag/AgCl respectively, which could be attributed to the redox reactions of copper species inserted into two different coordination sites, the free carboxylate and the defected Zr cluster[77, 78]. UiO-66-$(COOH)_2$Cu shows a higher voltametric current than UiO-66-$(COOH)_2$, indicating better conductivity and improved electron/ion mobility. Furthermore, Electrochemical Impedance spectroscopy (EIS) was employed to deduce an insight about the charge transfer resistance and the response of the system under various frequency regimes[79]. UiO-66-$(COOH)_2$-Cu shows smaller charger transfer resistance with respect to UiO-66-$(COOH)_2$, which confirms the enhanced conductivity and better electron mobility in UiO-66-$(COOH)_2$-Cu (Figure S14B).

Restructuring phenomena as investigated by *operando* analysis of the photocatalyst surface

The evolution in real-time of the IR spectra of the photocatalysts surface has been monitored simultaneously with the gas phase analysis as previously mentioned using the IR *operando* setup[80]. As it can be seen in Figure 5A, a gradual increase with the reaction time of the bands intensity at 1855, 1798 and 1785 cm^{-1} on UiO66-$(COOH)_2$-Cu is observed, which corresponds to the anhydride formation (UiO66-$(COO)_2$-Cu). In addition, water released from the catalyst surface is simultaneously detected. In general, water molecules could be produced from the dehydration process of the formic acid. Nevertheless, the absence of CO in the gas phase suggests another origin of the water release which most likely results from the dehydration process of the carboxylate functions prior to the formation of bridging anhydrides in the first few minutes of irradiation as well as of the copper clustering, which will be discussed further in the XPS and HR-TEM analysis section. Once anhydrides reach a steady state, the hydrogen production attains also its steady state (Figure 5B). However, this trend was only observed in the first cycle showing the irreversible behavior of this restructuring process which leads to the formation of the highly active UiO66-$(COO)_2$-Cu photocatalyst.

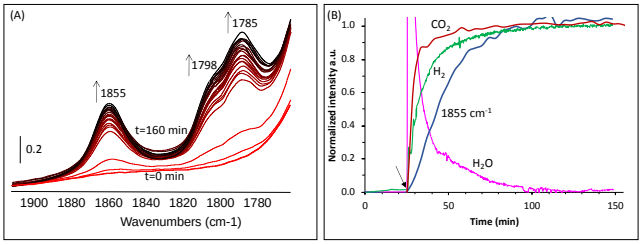

Figure 5. (A) FTIR spectra of UiO66-$(COO)_2$-Cu surface during the reforming of formic acid_C-13 under visible light irradiation. (B) Evolution of the corresponding normalized intensities of the gas phase products and the band area at 1855 cm^{-1} of the surface versus the irradiation time. Reaction condition: total flow = 25 cc/min; [Formic acid-^{13}C]=2400ppm (0.24%) in Ar; T=25°C; Xe-lamp 150 W with visible light pass filter (λ>390 nm); irradiance=71 mW/cm^2; m_{cat}=20 mg (self-supported pellet with surface of 1.6 cm^2). The arrow in (B) corresponds to the time of the light-ON.

To gain deep understanding on the restructuring process of UiO66-$(COOH)_2$-Cu to UiO66-$(COO)_2$-Cu and the formation of anhydride, a steady state isotopic transient kinetic analysis (SSITKA) experiment using FTIR *operando* spectroscopy was performed. It corresponds to replacing the formic acid by its isotope at the steady state under the same reaction conditions. This isotopic transient would induce a shift/modification on the mass spectrometry signals and/or of the IR vibration bands of the corresponding products as well as of the species adsorbed on the analyzed surface. Therefore, as the IR bands of carboxylate functions of the formic acid and of the UiO66-$(COOH)_2$-Cu's ligand could overlap, this experiment allows distinguishing the origin of the final products as well as of the anhydride. The so-obtained results are shown in Figure 6 and illustrate the kinetic of the reaction in gas phase and of the adsorbed surface species during the SSITKA experiment. Contrarily to the shift and the isotopic exchange observed for the gas phase products (Figures 6 A, B and E) and for the adsorbed formic acid (Figures 6C and F), no perturbation of the bands position at 1855 cm^{-1} and 1784 cm^{-1} is observed (Figures 6D, F and S15). These results indicate that the anhydride formation resulted from a selective cross-coupling of the MOF carboxylate linkers. Nevertheless, these bands are not observed during the pre-activation of the photocatalyst under inert carrier gas and

are only detected during reaction. Therefore, an indirect role of the formic acid in the anhydride formation cannot be excluded. In addition, the corresponding IR-bands of anhydride functions are not observed when Cu-free UiO66-$(COOH)_2$ is employed as photocatalyst under similar reaction conditions, which clearly emphasizes the role of Cu in assisting the formation of anhydride in UiO66-$(COO)_2$ under visible light. Our hypothesis is that $HCOO^-H^+$ delivers protons to the metalated-carboxylate (COO-Cu-) functions of the ligand, promoting the formations of those anhydrides under irradiation. Furthermore, the position of these characteristic bands is shifted toward lower υ^{-1} values when compared to the free anhydrides formed by thermal treatment of UiO-66$(COOH)_2$[69] due to the insertion of copper cations.

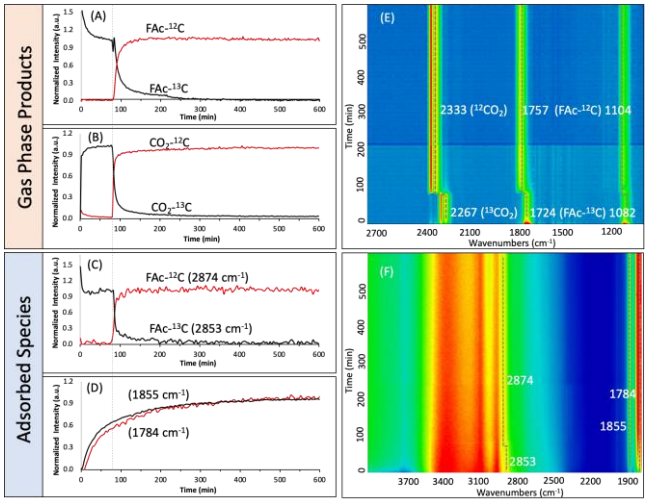

Figure 6. Evolution of gas phase products (A-B) and adsorbed species on UiO-66-$(COO)_2$-Cu (C-D) versus time of the FAc-^{13}C/FAc-^{12}C SSITKA experiment (t=0 corresponds to the irradiation's time and dotted line corresponds to the FAc-^{13}C/FAc-^{12}C). E and F correspond to the relative evolution on the IR intensities (from lower (blue color) to higher (red color)) of the reaction gas phase and photocatalyst surface, respectively. Reaction condition: total flow 25 cc/min; [FAc-^{13}C]=[FAc-^{12}C]=2400ppm (0.24%) in Ar; T=25°C; Xe-lamp 150 W with visible light pass filter (λ>390 nm); irradiance=71 mW/cm^2; m_{cat}=20 mg (self-supported pellet with surface of 1.6 cm^2).

The dehydrogenation of the DCOOH was further explored in order to gain first light on the hydrogen evolution during the first minutes of irradiation. The DH formation is expected as the main products of the dehydrogenation of DCOOH molecule in case that the dissociation is taking place on a single site. However, the obtained results depicted in Figure 7A show a mixture of hydrogen isotopes with a ratio of H_2/HD/D_2 swapped from 0.46/0.43/0.11 after 20 minutes of reaction to 0.35/0.5/0.15 at the steady state. The formation of the H_2 and D_2 confirms that the dissociation occurs in multiple steps and/or on multiple sites. It can be attributed to the scrambling of the formate/formyl as we demonstrated in our previous work in the case of methanol photooxidation[66]. In addition, the evolution of the statistic values of the isotope ratios follows a similar trend to the anhydride bands (Figure 7B) suggesting different mechanism of the DCOOH decomposition at the steady state in respect to that at the beginning of the reaction, and therefore is coherent with the restructuration of the catalyst.

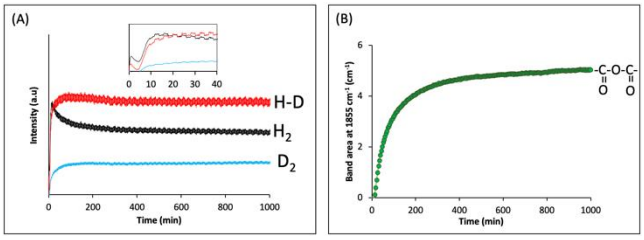

Figure 7. Evolution of the hydrogen isotopes (A) and of the anhydride vibration bands (B) during the photocatalytic dehydrogenation of DCOOH under visible light. Insert (A): zoom on the first 40 minutes of the reaction. Reaction condition: total flow 25 cc/min; [DCOOH]=2400ppm (0.24%) in Ar; T=25°C; Xe-lamp 150 W with visible light pass filter (λ>390 nm); irradiance=71 mW/cm^2; m_{cat}=20 mg (self-supported pellet with surface of 1.6 cm^2).

Restructuring phenomena as investigated by XPS and HR-TEM-EDX analyses

More insight on the restructuring process of the catalyst during the reaction is obtained from SEM-EDX mapping, AA, XPS and HR-TEM-EDX mapping analyses of the material before and after the photocatalytic reaction tests. The SEM images and the EDX mapping (Figure S16) of the samples before and after reaction demonstrate small modification on the gradual concentration of the Cu. However, no modification of the Cu/Zr ratio (0.75) and copper content (19 wt.%) are detected in line with the elemental analysis of the samples using the atomic absorption (AA) techniques (Figure S17). On the other hand, the XPS analysis of the two samples demonstrates a very significant decrease after reaction (around 8 times) of the Cu/Zr ratio from 4.1 to 0.5 (Figures S18 and S19). This deviation between the EDX and XPS analysis data could be explained by the limited penetration of the XPS beam in the samples (only few nm) while the EDX and AA analysis are more global.

Furthermore, the XPS analysis is performed for UiO-66-$(COOH)_2$ and for its metalated form before and after reaction (Figure 8, S18 and S19). The obtained data reveals information on the evolution of the oxidation state of the copper. The Cu 2p3/2 peak at 935.8 eV observed for UiO-66-(COO)-Cu could be assigned to $Cu^{(II)}$, with shake up peaks of 2p-to-3d observed between 940–945 eV while the more negative peak at 933 eV ascribed to $Cu^{(I)}$ was the main detected peak in the sample after reaction, The latter was assigned to Cu_2O formation, with a quasi-total disappearance of the highly coordinated $Cu^{(II)}$ species. Therefore, the absence of the Cu 2p satellite clearly indicates that after the reaction there are mainly $Cu^{(I)}$ species present (Figure 8). The results also demonstrate some perturbation on the range of Zr as well, which could be mainly assigned to some modifications of the Zr sites environment.

However, as the analysis was performed ex-situ, it was not possible to discuss the results quantitatively as the catalyst surface could change its state after exposure to the atmosphere (e.g. oxidation of the metal clusters). We strongly believe that the photogenerated electrons promote the reduction of $Cu^{(II)}$ to form lower oxidation state species (e.g. $Cu^{(I)}$ and/or $Cu^{(0)}$) during the reaction. The presence of the latter was confirmed by the diffuse reflectance spectra recorded for the UiO66-$(COO)_2$-Cu pellets freshly taken after the reaction and showed the typical broad absorption band of Cu_2O in the visible region (420 and 485 nm) in addition to a shoulder peak evolved at 625 nm mainly in the highly loaded sample which corresponds to the plasmonic band of Cu NPs[81] (Figure S20).

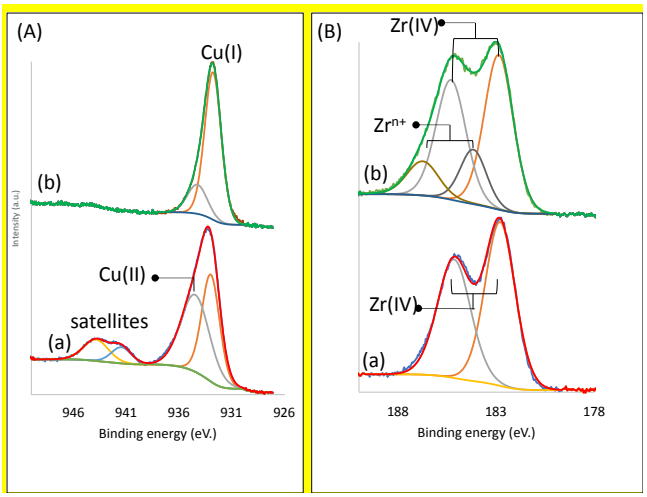

Figure 8. Cu2p$_{3/2}$ (A) and Zr3d (B) levels of UiO-66-$(COO)_2$-Cu before (a) and after reaction (b).

Transmission electron microscopy shed more light on the zoning phenomena of the copper before and after reaction. The obtained high angle annular dark field scanning TEM (HAADF-STEM) images in combination with STEM-EDX elemental mapping depicted in Figure 9(a and b), confirm a higher concentration of the copper clusters/atoms at the external surface of the UiO-66-$(COOH)_2$-Cu crystal before the reaction demonstrating a limited diffusion of the Cu(II) in the MOFs. After reaction, a formation of copper clusters inside the crystal with around 3-5 nm of size (core-shell form) can be clearly observed in HAADF-STEM image (bright contrast) (Fig 9c) and STEM – EDX elemental mapping (Fig. 9f). Despite that the metal sintering from the nanopores of a crystalline porous structure to its external surface is a very usual phenomenon already observed in the case of zeolites[70], to our knowledge, the opposite migration was never reported before. Moreover, no diffraction index of the copper oxide clusters is detected in agreement with the PXRD data (Figure SA). The selective area electron diffraction (SAED) pattern taken from single UiO-66-$(COO)_2$-Cu clusters after reaction revealed week diffraction rings (Fig. 9c inset) which can be indexed based on cubic Cu_2O structure (Pn-3m, a=0.426 nm ICSD 172174). This could be attributed to the Cu-oxo like species formed during the in-situ restructuring of $Cu^{(II)}$ under the reaction and stabilized by an electrostatic interaction with the remained carboxylate defects of the structure. Nevertheless, no ex-site detection of $Cu^{(0)}$ NPs was observed and probably to the high dispersion of this later and their low stability after exposing the sample to air condition. However, similar in situ restructuring process has been recently demonstrated for the CuO-TiO_2 and CuO-Nb_3O_7(OH) systems[82].In these hetero-nanostructures, the non-active CuO-TiO_2 and CuO-Nb_3O_7(OH) undergo reduction reactions under light irradiation to form the active Cu_2O-TiO_2 and Cu(0)-Nb_3O_7(OH), respectively. The formation of $Cu^{(0)}$ is as well demonstrated by using the Cu_2O which illustrate a 2h of induction time assigned to the in-situ formation of $Cu^{(0)}$ NPs. The copper clustering process is in agreement with the release of water detected by *operando* analysis, which could be assigned for both dehydration of carboxylate and of CuOH groups. Furthermore, the high resolution HAADF–STEM imaging (Fig. 9d) and high-resolution TEM (Fig. 9e) confirmed the Cu_2O structure of clusters and UiO66 structure of the framework. Image of the 002 lattice planes in the shell of the UiO66-$(COO)_2$-Cu particle (Fig.9e) suggests that structure of the UiO66 stay intact after Cu diffusion. Moreover, the analysis of the UiO66-Cu sample, used as reference in which copper is anchored within the Zr-defective clusters demonstrates a total deterioration of the crystal after only a few hours of the reaction (10 h) (Figure S21). A total structure destruction accompanied by the formation of Cu nanoparticles is confirmed by PXRD pattern of the UiO-66-Cu sample after reaction (Figure S22). These interesting results reveal a crucial role of the bridged anhydrides in preserving the UiO66-$(COO)_2$-Cu crystallinity and therefore demonstrate the high stability of this photocatalyst. In addition, the anhydride bridges could form a cage-like structures around copper clusters preventing the migration of the particles and further stabilize the UiO66 structure.

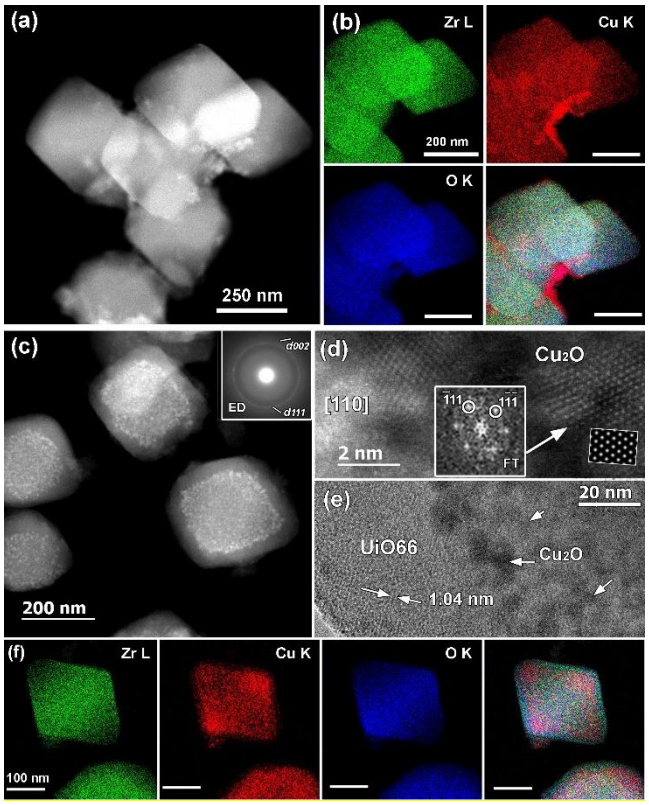

Figure 9. (a) HAADF-STEM image of UiO-66-$(COOH)_2$-Cu material and (b) corresponding EDX-STEM elemental mapping for Zr L(green), Cu K (red), O K (blue) and overlaid color image before reaction; (c) HAADF-STEM image of UiO-66-$(COO)_2$-Cu obtained after reaction with the corresponding ring ED pattern indexed based on cubic *Pn-3m* structure of Cu_2O; (d) high resolution HAADF-STEM image of Cu based nanoparticles formed after the reaction and assigned to Cu_2O. Inset: corresponding [110] FT pattern indexed based on cubic Cu_2O cubic structure, and simulated [110]HAADF-STEM images in the white box showing good fitting to the experimental image. (e) bright field HRTEM image of the edge of UiO-66-$(COO)_2$-Cu nanoparticle after reaction. The Cu_2O NPs exhibit a black contrast, marked with white arrows. Noticed free of Cu near surface region of UiO-66-$(COO)_2$-Cu nanoparticles; (f) EDX-STEM elemental mapping of UiO-66-$(COO)_2$-Cu particles after reaction for Zr L(green), Cu K (red), O K (blue) and overlaid color image showing the diffusion of the copper element inside the UiO-66-$(COO)_2$-Cu framework.

Complementary microscopic insight into the reaction mechanism by DFT calculations

DFT calculations first explored the preferential geometry of the UiO66-$(COO)_2$-Cu system starting with the experimental conclusions that Cu-assists the dehydration of the carboxylic groups. Figure S1 reports a representation of the two-coordinated Cu(I) configuration with the surrounding oxygen atoms of the anhydride group in the DFT-optimized cluster model of UiO-66-$(COO)_2$-Cu. Due to the complexity of the structure, only a single copper site and its environment is considered for the DFT calculation. It is noteworthy that this model complex was observed experimentally through the in-situ FTIR measurements discussed earlier. As a further step, the minimum energy reaction pathway was explored for the dehydrogenation of formic acid by UiO-66-$(COO)_2$-Cu throughout the HCOO-dehydrogenation (Figure 10A) and COOH-dehydrogenation (Figure S23) routes. The first step of the HCOO-dehydrogenation reaction proceeds *via* the coordination of the HCOOH molecule towards the Cu site (Figure 10B) associated with a high adsorption energy of -1.53 eV and a large fraction of electrons accumulated along the Cu-O(CO) bond (Figure S24). The adsorbed HCOOH molecule (labeled as HCOOH*) then undergoes O–H bond cleavage *via* the formation of a first transition state (TS1) corresponding to an energy barrier of 0.53 eV that leads to the formation of HCOO* and H*. This intermediate species evolves towards a second transition state (TS2) with an energy barrier of 0.83 eV prior to form CO_2 as well as 2H* which subsequently dehydrogenates *via* a third transition state (TS3) accompanied with an energy barrier of 0.59 eV to further release a gas-phase H_2 molecule.

Regarding the COOH-dehydrogenation pathway, the adsorption configuration of HCOOH molecule corresponds to a metastable state with the corresponding adsorption energy of -1.27 eV, compared to the adsorption configuration of HCOOH molecule by HCOO-dehydrogenation mechanism (Figures S23-S24). Next, the intermediate COOH* and H* species is formed *via* a C–H bond breaking (TS1-energy barrier of 1.13 eV) followed by the formation of COOH** *via* TS2 (energy barrier of 0.58 eV) and its further transferred to HCOO' and 2H*. Then HCOO' dehydrogenates *via* TS3 with a barrier of 1.12 eV to produce CO_2 and 2H* intermediate. Finally, the adsorbed H* intermediate is released from the Cu site to form H_2. For HCOO-dehydrogenation pathway, the rate-determining step (RDS) is the transformation of HCOOH* + H* to 2H* + CO_2 with an energy barrier of 0.83 eV, while the formation of H* + HOOC is the RDS for the COOH-dehydrogenation (energy barrier: 1.13 eV). This observation suggests that the HCOO-dehydrogenation pathway is more plausible. Remarkably, in the final product, Cu still keeps its original two-coordinated geometry and its (+1) oxidation state to further adsorb another HCOOH molecule to initiate a second dehydrogenation cycle, which is also consistent with what was observed experimentally. It should be noted that the Cu clusters could coordinate with the formate of the formic acid as well as with the unbridged carboxylates of MOF structure. Another plausible pathway can be suggested based on our experimental findings and it is strongly related to the reaction mechanisms reported on traditional hetero-nanostructured photocatalysts (scheme 1). After the formation of anhydride-Cu(I) during the reaction, a nanoclustering process leads to the formation of Cu_2O Nps which were observed during the HRTEM and XPS analysis of the samples after reaction and in agreement with the release of water detected by *operando* analysis. The surface $Cu^{(I)}$ particles undergo further reduction through the photogenerated electrons which results in the formation of $Cu^{(0)}$ clusters that act as electrons' pool for the reduction of proton into H_2. Although, $Cu^{(0)}$ clusters are not efficient in photocatalysis when they are isolated as single metal particles, their photo-activity in our system can be explained

by the photo-sensibilization and/or charge transfer pathways through their strong interactions with the anhydride units and with Cu_2O nanostructure surface. In addition, the anhydride functions play a crucial role as stabilizers of the Cu and $Cu^{(I)}$ oxo particles during the reaction according to the notable high stability of the UiO66-$(COO)_2$-Cu photocatalyst.

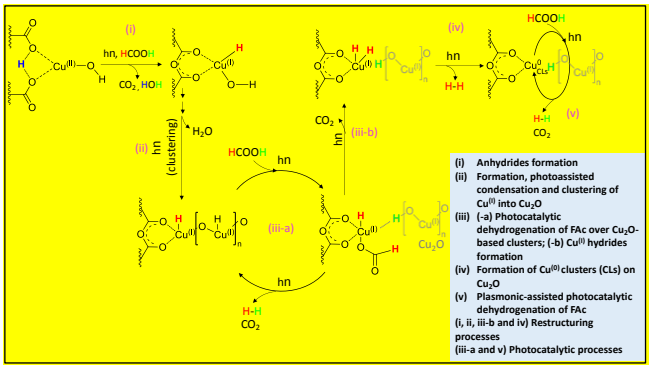

Scheme S1. Plausible restructuring pathways of UiO-66-(COOH)2-Cu during the FAc reforming under visible light leading to the formation of supported and stabilized Cu(0)/Cu(I) binary system on UiO66-(COO)2.

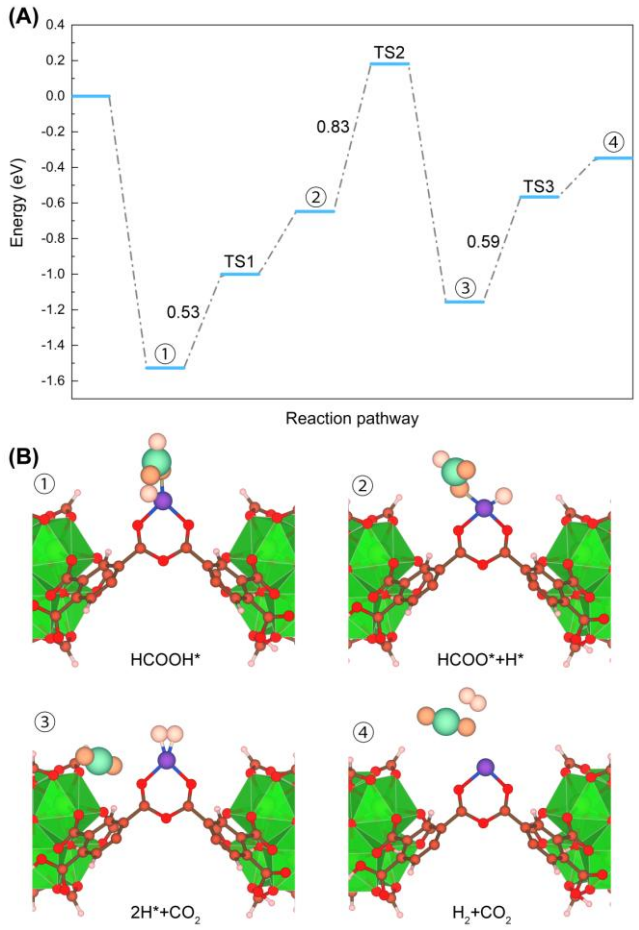

Figure 10. (A) DFT-derived minimum energy pathway for the dehydrogenation of formic acid by UiO-66-$(COO)_2$-Cu and (B) corresponding illustrative snapshots of the different intermediate species. The energy barriers (expressed in eV) for the 3 transition states (TS) are also shown in the figure. Color codes for the MOF: C, gray; Cu, blue; O, red; H, white; Zr, green. Color codes for the adsorbed molecules: C, light blue; O, orange; H, white. The total free energy of UiO-66-$(COO)_2$-Cu structure with gas-phase HCOOH molecule is set as the zero in the Gibbs free energy profile.

Conclusion:

In summary, a copper metalated based metal organic framework, namely UiO-66-$(COO)_2$-Cu was engineered, fully characterized, and employed as photocatalyst for the dehydrogenation of formic acid. This rare-noble-metal free catalyst was demonstrated to be highly selective (>99.99%), stable (3 days of reaction), and efficient at room temperature with a high formic acid dehydrogenation (4.8 $mmol.g^{-1}_{cat}.h^{-1}$). The high performance and stability of the UiO-66-$(COO)_2$-Cu compared with the standard copper metalated UiO-66-Cu was attributed to the *in-situ* restructuring process taking place at the surface of the former through intra-framework cross-linking resulted in the formation of highly active Cu_2O NPs trapped in the UiO66 cages. This study opens the way for designing new Cu based MOF for various application in photocatalysis. It allows highlighting the mechanism inside the formic acid dehydrogenation, a potential intermediate in several reaction such as the CO_2 reduction.

ASSOCIATED CONTENT

Supporting Information. Synthesis and characterization of the MOF catalysts, including PXRD patterns, UV-visible, IR spectra, Raman Spectroscopy, SEM-EDX mapping, Atomic Absorbance, XPS Analysis, CV, EIS, and DFT calculations. "This material is available free of charge via the Internet at http://pubs.acs.org."

AUTHOR INFORMATION

Corresponding Author

*mohamad.elroz@ensicaen.fr
*mohamad.hmadeh@aub.edu.lb

ACKNOWLEDGMENT

Mohamad El-Roz and Houeida Issa Hamoud acknowledge the Normandy region (RIN Research 2020 – Emergent: H_2CO_2 project) for the financial support.
MH acknowledges the grant provided by the American University Research Board (URB) and the Arab Fund Fellowship Program.

REFERENCES

1. Lubitz, W.; Tumas, W., Hydrogen: An Overview. *Chemical Reviews* **2007,** *107* (10), 3900-3903.
2. Megía, P. J.; Vizcaíno, A. J.; Calles, J. A.; Carrero, A., Hydrogen Production Technologies: From Fossil Fuels toward Renewable Sources. A Mini Review. *Energy & Fuels* **2021,** *35* (20), 16403-16415.

3. Lam, M. K.; Lee, K. T., Renewable and sustainable bioenergies production from palm oil mill effluent (POME): Win–win strategies toward better environmental protection. *Biotechnology Advances* **2011,** *29* (1), 124-141.
4. Van Hoecke, L.; Laffineur, L.; Campe, R.; Perreault, P.; Verbruggen, S. W.; Lenaerts, S., Challenges in the use of hydrogen for maritime applications. *Energy & Environmental Science* **2021,** *14* (2), 815-843.
5. Navlani-García, M.; Mori, K.; Kuwahara, Y.; Yamashita, H., Recent strategies targeting efficient hydrogen production from chemical hydrogen storage materials over carbon-supported catalysts. *NPG Asia materials* **2018,** *10* (4), 277-292.
6. Deng, Y.; Guo, Y.; Jia, Z.; Liu, J.-C.; Guo, J.; Cai, X.; Dong, C.; Wang, M.; Li, C.; Diao, J.; Jiang, Z.; Xie, J.; Wang, N.; Xiao, H.; Xu, B.; Zhang, H.; Liu, H.; Li, J.; Ma, D., Few-Atom Pt Ensembles Enable Efficient Catalytic Cyclohexane Dehydrogenation for Hydrogen Production. *Journal of the American Chemical Society* **2022,** *144* (8), 3535-3542.
7. Schlapbach, L.; Züttel, A., Hydrogen-storage materials for mobile applications. *Nature* **2001,** *414* (6861), 353-358.
8. Yadav, M.; Xu, Q., Liquid-phase chemical hydrogen storage materials. *Energy & Environmental Science* **2012,** *5* (12), 9698-9725.
9. Demirci, U. B.; Miele, P., Chemical hydrogen storage: 'material' gravimetric capacity versus 'system' gravimetric capacity. *Energy & Environmental Science* **2011,** *4* (9), 3334-3341.
10. Yang, Z.; Xia, Y.; Mokaya, R., Enhanced Hydrogen Storage Capacity of High Surface Area Zeolite-like Carbon Materials. *Journal of the American Chemical Society* **2007,** *129* (6), 1673-1679.
11. Lee, H.; Lee, J.-w.; Kim, D. Y.; Park, J.; Seo, Y.-T.; Zeng, H.; Moudrakovski, I. L.; Ratcliffe, C. I.; Ripmeester, J. A., Tuning clathrate hydrates for hydrogen storage. *Nature* **2005,** *434* (7034), 743-746.
12. Kato, R.; Nishide, H., Polymers for carrying and storing hydrogen. *Polymer Journal* **2018,** *50* (1), 77-82.
13. Singh, A. K.; Singh, S.; Kumar, A., Hydrogen energy future with formic acid: a renewable chemical hydrogen storage system. *Catalysis Science & Technology* **2016,** *6* (1), 12-40.
14. Schneemann, A.; White, J. L.; Kang, S.; Jeong, S.; Wan, L. F.; Cho, E. S.; Heo, T. W.; Prendergast, D.; Urban, J. J.; Wood, B. C.; Allendorf, M. D.; Stavila, V., Nanostructured Metal Hydrides for Hydrogen Storage. *Chemical Reviews* **2018,** *118* (22), 10775-10839.
15. Singh, S. K.; Xu, Q., Complete Conversion of Hydrous Hydrazine to Hydrogen at Room Temperature for Chemical Hydrogen Storage. *Journal of the American Chemical Society* **2009,** *131* (50), 18032-18033.
16. White, J. L.; Baker, A. A.; Marcus, M. A.; Snider, J. L.; Wang, T. C.; Lee, J. R. I.; Kilcoyne, D. A. L.; Allendorf, M. D.; Stavila, V.; El Gabaly, F., Hydrogen Storage: The Inside-Outs of Metal Hydride Dehydrogenation: Imaging the Phase Evolution of the Li-N-H Hydrogen Storage System (Adv. Mater. Interfaces 7/2020). *Advanced Materials Interfaces* **2020,** *7* (7), 2070034.
17. Chen, X.; Gierlich, C. H.; Schötz, S.; Blaumeiser, D.; Bauer, T.; Libuda, J.; Palkovits, R., Hydrogen Production Based on Liquid Organic Hydrogen Carriers through Sulfur Doped Platinum Catalysts Supported on TiO2. *ACS Sustainable Chemistry & Engineering* **2021,** *9* (19), 6561-6573.
18. Dalebrook, A. F.; Gan, W.; Grasemann, M.; Moret, S.; Laurenczy, G., Hydrogen storage: beyond conventional methods. *Chemical Communications* **2013,** *49* (78), 8735-8751.
19. Nikolaidis, P.; Poullikkas, A., A comparative overview of hydrogen production processes. *Renewable and Sustainable Energy Reviews* **2017,** *67*, 597-611.
20. Han, J.-R.; Park, S.-J.; Kim, H.; Lee, S.; Lee, J. M., Centralized and distributed hydrogen production using steam reforming: challenges and perspectives. *Sustainable Energy & Fuels* **2022,** *6* (8), 1923-1939.
21. Valentini, F.; Kozell, V.; Petrucci, C.; Marrocchi, A.; Gu, Y.; Gelman, D.; Vaccaro, L., Formic acid, a biomass-derived source of energy and hydrogen for biomass upgrading. *Energy & Environmental Science* **2019,** *12* (9), 2646-2664.
22. Nakajima, T.; Kamiryo, Y.; Kishimoto, M.; Imai, K.; Nakamae, K.; Ura, Y.; Tanase, T., Synergistic Cu2 Catalysts for Formic Acid Dehydrogenation. *Journal of the American Chemical Society* **2019,** *141* (22), 8732-8736.
23. Eppinger, J. r.; Huang, K.-W., Formic Acid as a Hydrogen Energy Carrier. *ACS energy letters* **2017,** *2* (1), 188-195.
24. Müller, K.; Brooks, K.; Autrey, T., Hydrogen Storage in Formic Acid: A Comparison of Process Options. *Energy & Fuels* **2017,** *31* (11), 12603-12611.
25. Andersson, J.; Grönkvist, S., Large-scale storage of hydrogen. *International Journal of Hydrogen Energy* **2019,** *44* (23), 11901-11919.
26. Müller, K.; Brooks, K.; Autrey, T., Releasing Hydrogen at High Pressures from Liquid Carriers: Aspects for the H2 Delivery to Fueling Stations. *Energy & Fuels* **2018,** *32* (9), 10008-10015.
27. Fellay, C.; Dyson, P. J.; Laurenczy, G., A Viable Hydrogen-Storage System Based On Selective Formic Acid Decomposition with a Ruthenium Catalyst. *Angewandte Chemie International Edition* **2008,** *47* (21), 3966-3968.
28. Iguchi, M.; Himeda, Y.; Manaka, Y.; Matsuoka, K.; Kawanami, H., Simple Continuous High-Pressure Hydrogen Production and Separation System from Formic Acid under Mild Temperatures. *ChemCatChem* **2016,** *8* (5), 886-890.
29. Greeley, J.; Mavrikakis, M., Competitive Paths for Methanol Decomposition on Pt(111). *Journal of the American Chemical Society* **2004,** *126* (12), 3910-3919.
30. Turco, M.; Bagnasco, G.; Cammarano, C.; Senese, P.; Costantino, U.; Sisani, M., Cu/ZnO/Al2O3 catalysts for oxidative steam reforming of methanol: The role of Cu and the dispersing oxide matrix. *Applied Catalysis B: Environmental* **2007,** *77* (1), 46-57.
31. Zhang, L.; Yu, Z.; Li, J.; Zhang, S.; Hu, S.; Xiang, J.; Wang, Y.; Liu, Q.; Hu, G.; Hu, X., Steam reforming of typical small organics derived from bio-oil: Correlation of their reaction behaviors with molecular structures. *Fuel* **2020,** *259*, 116214.
32. Kanega, R.; Ertem, M. Z.; Onishi, N.; Szalda, D. J.; Fujita, E.; Himeda, Y., CO2 Hydrogenation and Formic Acid Dehydrogenation Using Ir Catalysts with Amide-Based Ligands. *Organometallics* **2020,** *39* (9), 1519-1531.

33. Tanaka, R.; Yamashita, M.; Nozaki, K., Catalytic Hydrogenation of Carbon Dioxide Using Ir(III)−Pincer Complexes. *Journal of the American Chemical Society* **2009,** *131* (40), 14168-14169.
34. Ahlquist, M. S. G., Iridium catalyzed hydrogenation of CO2 under basic conditions—Mechanistic insight from theory. *Journal of Molecular Catalysis A: Chemical* **2010,** *324* (1), 3-8.
35. Baschuk, J. J.; Li, X., Carbon monoxide poisoning of proton exchange membrane fuel cells. *International Journal of Energy Research* **2001,** *25* (8), 695-713.
36. Matsunami, A.; Kuwata, S.; Kayaki, Y., A Bifunctional Iridium Catalyst Modified for Persistent Hydrogen Generation from Formic Acid: Understanding Deactivation via Cyclometalation of a 1,2-Diphenylethylenediamine Motif. *ACS Catalysis* **2017,** *7* (7), 4479-4484.
37. Yuranov, I.; Autissier, N.; Sordakis, K.; Dalebrook, A. F.; Grasemann, M.; Orava, V.; Cendula, P.; Gubler, L.; Laurenczy, G., Heterogeneous Catalytic Reactor for Hydrogen Production from Formic Acid and Its Use in Polymer Electrolyte Fuel Cells. *ACS Sustainable Chemistry & Engineering* **2018,** *6* (5), 6635-6643.
38. Zhu, Q.-L.; Xu, Q., Liquid organic and inorganic chemical hydrides for high-capacity hydrogen storage. *Energy & Environmental Science* **2015,** *8* (2), 478-512.
39. Coffey, R. S., The decomposition of formic acid catalysed by soluble metal complexes. *Chemical Communications (London)* **1967,** (18), 923b-924.
40. Huang, Y.; Zhou, X.; Yin, M.; Liu, C.; Xing, W., Novel PdAu@Au/C Core−Shell Catalyst: Superior Activity and Selectivity in Formic Acid Decomposition for Hydrogen Generation. *Chemistry of materials* **2010,** *22* (18), 5122-5128.
41. Bandara, A.; Kubota, J.; Wada, A.; Domen, K.; Hirose, C., Adsorption and Reactions of Formic Acid on (2×2)-NiO(111)/Ni(111) Surface. 2. IRAS Study under Catalytic Steady-State Conditions. *The Journal of Physical Chemistry B* **1997,** *101* (3), 361-368.
42. Ojeda, M.; Iglesia, E., Formic Acid Dehydrogenation on Au-Based Catalysts at Near-Ambient Temperatures. *Angewandte Chemie International Edition* **2009,** *48* (26), 4800-4803.
43. Bulushev, D. A.; Jia, L.; Beloshapkin, S.; Ross, J. R. H., Improved hydrogen production from formic acid on a Pd/C catalyst doped by potassium. *Chemical Communications* **2012,** *48* (35), 4184-4186.
44. Caiti, M.; Padovan, D.; Hammond, C., Continuous Production of Hydrogen from Formic Acid Decomposition Over Heterogeneous Nanoparticle Catalysts: From Batch to Continuous Flow. *ACS catalysis* **2019,** *9* (10), 9188-9198.
45. Xu, P.; Bernal-Juan, F. D.; Lefferts, L., Effect of oxygen on formic acid decomposition over Pd catalyst. *Journal of Catalysis* **2021,** *394*, 342-352.
46. Yu, X.; Pickup, P. G., Mechanistic study of the deactivation of carbon supported Pd during formic acid oxidation. *Electrochemistry Communications* **2009,** *11* (10), 2012-2014.
47. Petrik, N. G.; Wang, Y.; Wen, B.; Wu, Y.; Ma, R.; Dahal, A.; Gao, F.; Rousseau, R.; Wang, Y.; Kimmel, G. A.; Selloni, A.; Dohnálek, Z., Conversion of Formic Acid on Single- and Nano-Crystalline Anatase TiO2(101). *The Journal of Physical Chemistry C* **2021,** *125* (14), 7686-7700.
48. Henderson, M. A., Complexity in the Decomposition of Formic Acid on the TiO2(110) Surface. *The Journal of Physical Chemistry B* **1997,** *101* (2), 221-229.
49. Yaghi, O. M.; Li, H., Hydrothermal Synthesis of a Metal-Organic Framework Containing Large Rectangular Channels. *Journal of the American Chemical Society* **1995,** *117* (41), 10401-10402.
50. Kitagawa, S.; Kitaura, R.; Noro, S.-i., Functional Porous Coordination Polymers. *Angewandte Chemie International Edition* **2004,** *43* (18), 2334-2375.
51. Férey, G., Hybrid porous solids: past, present, future. *Chemical Society Reviews* **2008,** *37* (1), 191-214.
52. Ko, M.; Mendecki, L.; Eagleton, A. M.; Durbin, C. G.; Stolz, R. M.; Meng, Z.; Mirica, K. A., Employing Conductive Metal–Organic Frameworks for Voltammetric Detection of Neurochemicals. *Journal of the American Chemical Society* **2020,** *142* (27), 11717-11733.
53. Maurin, G.; Serre, C.; Cooper, A.; Férey, G., The new age of MOFs and of their porous-related solids. *Chemical Society Reviews* **2017,** *46* (11), 3104-3107.
54. Elcheikh Mahmoud, M.; Audi, H.; Assoud, A.; Ghaddar, T. H.; Hmadeh, M., Metal–Organic Framework Photocatalyst Incorporating Bis(4′-(4-carboxyphenyl)-terpyridine)ruthenium(II) for Visible-Light-Driven Carbon Dioxide Reduction. *Journal of the American Chemical Society* **2019,** *141* (17), 7115-7121.
55. Peralta, R. A.; Huxley, M. T.; Evans, J. D.; Fallon, T.; Cao, H.; He, M.; Zhao, X. S.; Agnoli, S.; Sumby, C. J.; Doonan, C. J., Highly Active Gas Phase Organometallic Catalysis Supported Within Metal–Organic Framework Pores. *Journal of the American Chemical Society* **2020,** *142* (31), 13533-13543.
56. Comito, R. J.; Fritzsching, K. J.; Sundell, B. J.; Schmidt-Rohr, K.; Dincă, M., Single-Site Heterogeneous Catalysts for Olefin Polymerization Enabled by Cation Exchange in a Metal-Organic Framework. *Journal of the American Chemical Society* **2016,** *138* (32), 10232-10237.
57. De, S.; Ould-Chikh, S.; Aguilar, A.; Hazemann, J.-L.; Zitolo, A.; Ramirez, A.; Telalovic, S.; Gascon, J., Stable Cr-MFI Catalysts for the Nonoxidative Dehydrogenation of Ethane: Catalytic Performance and Nature of the Active Sites. *ACS Catalysis* **2021,** *11* (7), 3988-3995.
58. Zhang, J.; An, B.; Li, Z.; Cao, Y.; Dai, Y.; Wang, W.; Zeng, L.; Lin, W.; Wang, C., Neighboring Zn–Zr Sites in a Metal–Organic Framework for CO2 Hydrogenation. *Journal of the American Chemical Society* **2021,** *143* (23), 8829-8837.
59. Marquez, C.; Simonov, A.; Wharmby, M. T.; Van Goethem, C.; Vankelecom, I.; Bueken, B.; Krajnc, A.; Mali, G.; De Vos, D.; De Baerdemaeker, T., Layered Zn2[Co(CN)6](CH3COO) double metal cyanide: a two-dimensional DMC phase with excellent catalytic performance. *Chemical Science* **2019,** *10* (18), 4868-4875.
60. Wang, S.; Cabrero-Antonino, M.; Navalón, S.; Cao, C.-c.; Tissot, A.; Dovgaliuk, I.; Marrot, J.; Martineau-Corcos, C.; Yu, L.; Wang, H.; Shepard, W.; García, H.; Serre, C., A Robust Titanium Isophthalate Metal-Organic Framework for Visible-Light Photocatalytic CO2 Methanation. *Chem* **2020,** *6* (12), 3409-3427.

61. Rogge, S. M. J.; Bavykina, A.; Hajek, J.; Garcia, H.; Olivos-Suarez, A. I.; Sepúlveda-Escribano, A.; Vimont, A.; Clet, G.; Bazin, P.; Kapteijn, F.; Daturi, M.; Ramos-Fernandez, E. V.; Llabrés i Xamena, F. X.; Van Speybroeck, V.; Gascon, J., Metal–organic and covalent organic frameworks as single-site catalysts. *Chemical Society Reviews* **2017,** *46* (11), 3134-3184.
62. Pascanu, V.; González Miera, G.; Inge, A. K.; Martín-Matute, B., Metal–Organic Frameworks as Catalysts for Organic Synthesis: A Critical Perspective. *Journal of the American Chemical Society* **2019,** *141* (18), 7223-7234.
63. Yang, D.; Gates, B. C., Catalysis by Metal Organic Frameworks: Perspective and Suggestions for Future Research. *ACS Catalysis* **2019,** *9* (3), 1779-1798.
64. Gu, X.; Lu, Z.-H.; Jiang, H.-L.; Akita, T.; Xu, Q., Synergistic Catalysis of Metal–Organic Framework-Immobilized Au–Pd Nanoparticles in Dehydrogenation of Formic Acid for Chemical Hydrogen Storage. *Journal of the American Chemical Society* **2011,** *133* (31), 11822-11825.
65. Martis, M.; Mori, K.; Fujiwara, K.; Ahn, W.-S.; Yamashita, H., Amine-Functionalized MIL-125 with Imbedded Palladium Nanoparticles as an Efficient Catalyst for Dehydrogenation of Formic Acid at Ambient Temperature. *The Journal of Physical Chemistry C* **2013,** *117* (44), 22805-22810.
66. Boddien, A.; Mellmann, D.; Gärtner, F.; Jackstell, R.; Junge, H.; Dyson, P. J.; Laurenczy, G.; Ludwig, R.; Beller, M., Efficient Dehydrogenation of Formic Acid Using an Iron Catalyst. *Science* **2011,** *333* (6050), 1733.
67. Beloqui Redondo, A.; Morel, F. L.; Ranocchiari, M.; van Bokhoven, J. A., Functionalized Ruthenium–Phosphine Metal–Organic Framework for Continuous Vapor-Phase Dehydrogenation of Formic Acid. *ACS Catalysis* **2015,** *5* (12), 7099-7103.
68. Mortada, B.; Matar, T. A.; Sakaya, A.; Atallah, H.; Kara Ali, Z.; Karam, P.; Hmadeh, M., Postmetalated Zirconium Metal Organic Frameworks as a Highly Potent Bactericide. *Inorganic Chemistry* **2017,** *56* (8), 4739-4744.
69. Ragon, F.; Campo, B.; Yang, Q.; Martineau, C.; Wiersum, A. D.; Lago, A.; Guillerm, V.; Hemsley, C.; Eubank, J. F.; Vishnuvarthan, M.; Taulelle, F.; Horcajada, P.; Vimont, A.; Llewellyn, P. L.; Daturi, M.; Devautour-Vinot, S.; Maurin, G.; Serre, C.; Devic, T.; Clet, G., Acid-functionalized UiO-66(Zr) MOFs and their evolution after intra-framework cross-linking: structural features and sorption properties. *Journal of Materials Chemistry A* **2015,** *3* (7), 3294-3309.
70. Kresse, G.; Furthmüller, J., Efficient iterative schemes for ab initio total-energy calculations using a plane-wave basis set. *Physical Review B* **1996,** *54* (16), 11169-11186.
71. Perdew, J. P.; Burke, K.; Ernzerhof, M., Generalized Gradient Approximation Made Simple. *Physical Review Letters* **1996,** *77* (18), 3865-3868.
72. Grimme, S., Semiempirical GGA-type density functional constructed with a long-range dispersion correction. *Journal of Computational Chemistry* **2006,** *27* (15), 1787-1799.
73. Henkelman, G.; Uberuaga, B. P.; Jónsson, H., A climbing image nudged elastic band method for finding saddle points and minimum energy paths. *The Journal of Chemical Physics* **2000,** *113* (22), 9901-9904.
74. El-Roz, M.; Bazin, P.; Daturi, M.; Thibault-Starzyk, F., Operando Infrared (IR) Coupled to Steady-State Isotopic Transient Kinetic Analysis (SSITKA) for Photocatalysis: Reactivity and Mechanistic Studies. *ACS Catalysis* **2013,** *3* (12), 2790-2798.
75. Zhu, Y.; Zheng, J.; Ye, J.; Cui, Y.; Koh, K.; Kovarik, L.; Camaioni, D. M.; Fulton, J. L.; Truhlar, D. G.; Neurock, M.; Cramer, C. J.; Gutiérrez, O. Y.; Lercher, J. A., Copper-zirconia interfaces in UiO-66 enable selective catalytic hydrogenation of CO2 to methanol. *Nature Communications* **2020,** *11* (1), 5849.
76. Sudha, V.; Murugadoss, G.; Thangamuthu, R., Structural and morphological tuning of Cu-based metal oxide nanoparticles by a facile chemical method and highly electrochemical sensing of sulphite. *Scientific Reports* **2021,** *11* (1), 3413.
77. Chen, X.; Cai, Y.; Liang, R.; Tao, Y.; Wang, W.; Zhao, J.; Chen, X.; Li, H.; Zhang, D., NH2-UiO-66(Zr) with fast electron transfer routes for breaking down nitric oxide via photocatalysis. *Applied Catalysis B: Environmental* **2020,** *267*, 118687.
78. Kochem, A.; Gennarini, F.; Yemloul, M.; Orio, M.; Le Poul, N.; Rivière, E.; Giorgi, M.; Faure, B.; Le Mest, Y.; Réglier, M.; Simaan, A. J., Characterization of a Dinuclear Copper(II) Complex and Its Fleeting Mixed-Valent Copper(II)/Copper(III) Counterpart. *ChemPlusChem* **2017,** *82* (4), 615-624.
79. Vivier, V.; Orazem, M. E., Impedance Analysis of Electrochemical Systems. *Chemical Reviews* **2022,** *122* (12), 11131-11168.
80. El-Roz, M.; Kus, M.; Cool, P.; Thibault-Starzyk, F., New Operando IR Technique to Study the Photocatalytic Activity and Selectivity of TiO2 Nanotubes in Air Purification: Influence of Temperature, UV Intensity, and VOC Concentration. *The Journal of Physical Chemistry C* **2012,** *116* (24), 13252-13263.
81. Chen, L.; Zhang, Y.; Zhu, P.; Zhou, F.; Zeng, W.; Lu, D. D.; Sun, R.; Wong, C., Copper Salts Mediated Morphological Transformation of Cu2O from Cubes to Hierarchical Flower-like or Microspheres and Their Supercapacitors Performances. *Scientific Reports* **2015,** *5* (1), 9672.
82. Hmadeh, M.; Hoepfner, V.; Larios, E.; Liao, K.; Jia, J.; Jose-Yacaman, M.; Ozin, G. A., New Hydrogen-Evolution Heteronanostructured Photocatalysts: Pt-Nb3O7(OH) and Cu-Nb3O7(OH). *ChemSusChem* **2014,** *7* (8), 2104-2109.

TOC graphic

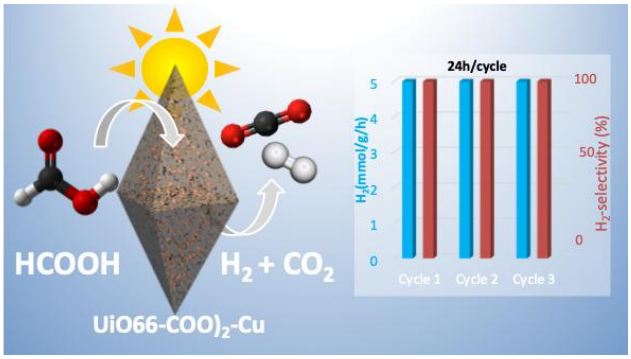
HCOOH
$H_2 + CO_2$
UiO66-COO)$_2$-Cu
24h/cycle
H_2(mmol/g/h)
H_2-selectivity (%)
0
1
2
3
4
5
0
50
100
Cycle 1
Cycle 2
Cycle 3